THE JOURNAL OF PHYSICAL CHEMISTRY C

pubs.acs.org/JPCC Article

Electron-Induced Reactions of $Ru(CO)_4I_2$: Gas Phase, Surface, and Electron Beam-Induced Deposition

Rachel M. Thorman,[‖] Pernille A. Jensen,[‖] Jo-Chi Yu, Scott J. Matsuda, Lisa McElwee-White, Oddur Ingólfsson, and D. Howard Fairbrother*

Cite This: *J. Phys. Chem. C* 2020, 124, 10593−10604 Read Online

ACCESS | Metrics & More | Article Recommendations | Supporting Information

ABSTRACT: The reactions of low energy (<100 eV) electrons with organometallic precursors underpin the fabrication of metal-containing nanostructures using focused electron beam-induced deposition. To understand these reactions at a molecular level, we have studied the electron-induced reactions of $Ru(CO)_4I_2$ in three different environments: as isolated molecules in the gas phase, adsorbed as thin films on surfaces, and as used in electron beam-induced deposition (EBID) in an Auger spectrometer. Gas-phase studies show that dissociative electron attachment (DEA) to $Ru(CO)_4I_2$ predominantly results in the loss of two CO ligands, while dissociative ionization (DI) of $Ru(CO)_4I_2$ leads to significantly more extensive fragmentation. Surface science studies of thin films of $Ru(CO)_4I_2$ adsorbed on gold at −100 °C and irradiated with 500 eV electrons show that decomposition proceeds in two distinct steps: (1) an initial loss of two CO ligands, followed by (2) a slower step, where the residual two CO ligands desorb, leaving RuI_2 on the surface. EBID using $Ru(CO)_4I_2$ and its brominated analogue, $Ru(CO)_4Br_2$, produced deposits with a ruthenium-to-halide ratio of ≈1:2 and minimal carbon and oxygen contamination. These results suggest that DEA is dominant over DI in the initial deposition step on the surface. This step produces a partially decarbonylated $Ru(CO)_2I_2$ species, which is then subject to CO desorption under further electron irradiation, findings likely generalizable to other $Ru(CO)_4X_2$ species (X = halide). The desorption of CO from the partially decarbonylated intermediate differs markedly from the results obtained for other metal carbonyls (e.g., $W(CO)_6$), a difference tentatively ascribed to the presence of M−X bonds.

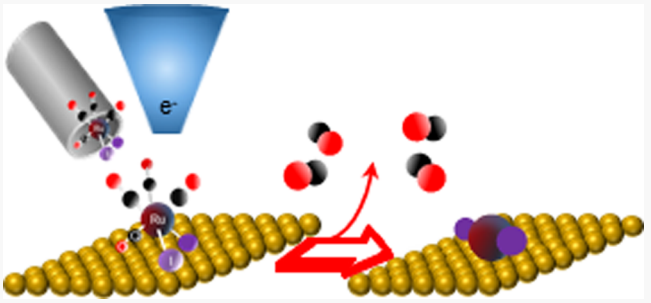

INTRODUCTION

Focused electron beam-induced deposition (FEBID) is a maskless, direct-write nanofabrication technique, which can be used to make three-dimensional nanoscale structures on nonplanar substrates.[1−4] Utilizing the narrow focus of a high-energy (1−30 keV) electron beam to create nanostructures, a lateral resolution of 3 nm has been achieved.[5] FEBID takes a fairly simple approach to creating and modifying nanostructures on a surface, making it an important technique for prototyping nanostructures for applications in nanoelectronics,[6] nanomagnetics,[7,8] nano-optics, plasmonics,[9,10] superconductors,[11,12] and sensing devices.[13−15] FEBID has also been used commercially to fabricate tips for magnetic force microscopy[16] and in the repair of photolithographic masks.[17] Deposition of Ru with FEBID may be of importance to extreme ultraviolet lithography (EUVL), where Ru is used as a capping layer in EUVL masks.[18]

In FEBID, a gaseous organometallic precursor is introduced into a high vacuum chamber equipped with a high-energy electron beam. The tightly focused electron beam, with typical energies between 1 and 30 keV, impacts the substrate, creating a plume of secondary electrons (SEs) which react with adsorbed precursor molecules to form a deposit. In the ideal situation, the precursor compound fully dissociates under the area of the tightly focused electron beam and the dissociated ligands are volatile enough to readily desorb from the surface, leaving a highly pure metallic deposit. However, current FEBID precursors are generally chosen from compounds developed for chemical vapor deposition (CVD), which is a thermally driven process rather than an electron-driven process. Due to being optimized for a different type of chemistry, some of the most common CVD precursors, such as, $MeCpPtMe_3$,[19−21] lead to incomplete decomposition and low-metal purity deposits.

Deposition in FEBID is generally considered to be derived from interactions between the precursor molecules and low-energy SEs generated by inelastic scattering of the high-energy

Received: February 29, 2020
Revised: April 10, 2020
Published: April 14, 2020

https://dx.doi.org/10.1021/acs.jpcc.0c01801
J. Phys. Chem. C 2020, 124, 10593−10604

electrons from the focused beam within the substrate and at its surface. The energy range of the SEs is typically defined as 0−100 eV.[2,22−25] Interactions with low-energy electrons (LEEs) are generally considered to be the driver for initial deposit formation and can lead to significant fragmentation but typically do not result in complete loss of all ligands, leading to organic contamination in the deposit.[19,20,26−28] Therefore, it is important to have a detailed understanding of how LEEs interact with potential FEBID precursors.

There are four distinct processes that can lead to fragmentation upon interaction between LEEs and molecules:[29]

Dissociative ionization (DI)

$$AB + e^- \rightarrow A^{(\#)+} + B^{(\#)} + 2e^- \quad (1)$$

Dissociative electron attachment (DEA)

$$AB + e^- \rightarrow AB^{(\#)-} \rightarrow A^{(\#)-} + B^{(\#)} \quad (2)$$

Neutral dissociation (ND)

$$AB + e^-(\varepsilon_1) \rightarrow [AB]^* + e^-(\varepsilon_2 < \varepsilon_1) \rightarrow A^{(\#)} + B^{(\#)} \quad (3)$$

Dipolar dissociation (DD)

$$AB + e^-(\varepsilon_1) \rightarrow [AB]^* + e^-(\varepsilon_2 < \varepsilon_1) \rightarrow A^{(\#)+} + B^{(\#)-} \quad (4)$$

Here, the hash (#) indicates that the molecule or fragment may be in an electronically and/or a vibrationally excited state and the asterisk (*) signifies that the molecule is in an electronically excited state. DI (eq 1) leads to a positively charged fragment and one or more neutral, generally radical fragments. It is a nonresonant process, generally with an onset slightly above the ionization threshold of the precursor molecule. The total cross section then increases with increasing incident electron energy until reaching a maximum, usually between 50 and 100 eV, before leveling off. As the energy of the electrons increases, the branching ratio shifts in favor of multiple bond ruptures. ND (eq 3) exhibits a similar threshold behavior to DI, but the onset is defined by the lowest antibonding electronic excitation above the dissociation limits of the respective bonds. It leads to two or more neutral fragments, which are usually radicals. DD (eq 4) proceeds in a similar manner to ND, but results in a negatively and positively charged fragment. It is less efficient than both DI and DEA and is also expected to be less efficient than ND. This is attributed to the Coulomb interaction of the two oppositely charged fragments.

DEA (eq 2) is, in contrast to the other processes discussed above, a resonant process. A transient negative ion is formed through electron attachment, which then relaxes through dissociation, forming a stable negative ion and one or more neutral (radical) fragments. The attachment proceeds in a narrow energy range defined by the Franck−Condon overlap between the neutral ground state and the negative potential energy surfaces of the respective anionic states formed in the process. Attachment is most efficient around 0 eV incident electron energy, and DEA is generally also most efficient at 0 eV as long as the respective processes are exothermic. Furthermore, DEA predominantly leads to specific bond breakage, forming a stable negative ion and a neutral radical. Each of the LEE processes described above (eqs 1−4) may contribute to the reactions that occur in FEBID, where the efficiency of each channel is expected to reflect a convolution of the energy dependence of the cross sections for the individual processes and the energy distribution of the available secondary LEEs.[23,30]

Unfortunately, it is not possible to directly study the effects of the secondary LEEs *in situ* in FEBID because precursor molecules are subjected simultaneously to a range of SEs with different energies. However, a combination of gas-phase and surface science studies can provide insight into these processes. In the current gas-phase studies, an effusive beam of precursor molecules is crossed with a beam of LEEs of well-defined energy, under single collision conditions, and the reaction products are monitored with a mass spectrometer.[29,31−33] Such studies can provide well-resolved information on LEE-induced reactions with precursor molecules, including accurate assessments of the branching ratios for individual DEA and DI fragmentation pathways and absolute cross sections.[19]

However, the single collision conditions of gas-phase experiments do not necessarily reflect the dissociation pathways of the same precursor molecules when interacting with a substrate. In order to gain more insight into the interactions of LEEs with precursors in FEBID, ultra-high vacuum (UHV) surface studies are performed wherein a film of adsorbed precursor molecules is subjected to a beam of 500 eV electrons. The fragments desorbing from the surface during electron irradiation are monitored with a mass spectrometer, while changes in the deposit during electron irradiation have been studied using X-ray photoelectron spectroscopy (XPS), reflection adsorption infrared spectroscopy, high-resolution electron energy loss spectroscopy, or a combination of the three.[34,35] By comparing the gas-phase and surface reactions of these precursor molecules, it is then possible to determine what type of interaction plays the largest role in the initial fragmentation of the adsorbed molecule and in what energy range the secondary LEEs contribute the most to contamination of the final deposit.[19] Comparative studies have been performed on a number of compounds, including $MeCpPtMe_3$,[19−21] $Pt(PF_3)_4$,[19,27,36−38] $Co(CO)_3NO$,[19,34,39] $W(CO)_6$,[19,28,40,41] $CpFe(CO)_2Mn(CO)_5$,[42,43] $(\eta^3\text{-}C_3H_5)Ru(CO)_3Br$,[44−46] $Pt(CO)_2Cl_2$,[47,48] $HFeCo_3(CO)_{12}$,[49,50] and $HFeRu_3(CO)_{13}$.[51] Through these comparative studies, it may be possible to identify the dominant initial dissociation mechanism. For example, for $MeCpPtMe_3$ adsorbed on a gold surface, the C/Pt ratio was observed to decrease from 9:1 to approximately 8:1, consistent with the single methyl loss observed in gas-phase DEA measurements.[19−21] Conversely, for $HFeRu_3(CO)_{13}$, an average of 8−9 CO ligands were lost in the initial electron irradiation of the adsorbed compound. Gas-phase measurements of this compound indicated an average CO loss of 0.5−3 per incident for DEA and 3−9 per incident for DI, strongly suggesting that DI was the dominant initial dissociation mechanism.

Here, we present comparative DEA and DI gas-phase and surface studies of a Ru-containing organometallic molecule, $Ru(CO)_4I_2$, and evaluate its potential as a FEBID precursor. Ruthenium has not previously been deposited at high purities,[46] possibly due to the use of precursors with significant carbon content (e.g., $(CpEt)_2Ru$ and $(\eta^3\text{-}C_3H_5)Ru(CO)_3Br$).[46,52] Previous studies of CO-containing precursors have shown that several CO ligands may desorb in the initial electron-mediated deposition step.[53] Furthermore, surface science experiments have shown that while halide ligands do not desorb during the initial electron-induced event, it is sometimes possible to remove them from surface layers of

https://dx.doi.org/10.1021/acs.jpcc.0c01801
J. Phys. Chem. C 2020, 124, 10593−10604

deposits by sustained electron irradiation (e.g., Cl removal from $Pt(CO)_2Cl_2$).[47,54] Halides can also be removed post-deposition, e.g., through thermal processing,[53] by subsequent exposure to atomic hydrogen,[54] or by annealing under forming gas.[46] These results suggest that FEBID using $Ru(CO)_4X_2$ may be a route to produce pure ruthenium deposits.

EXPERIMENTAL METHODS

Synthesis. *General.* Unless otherwise stated, all reactions were carried out under an inert atmosphere (N_2) using standard Schlenk techniques. Unless otherwise specified, all reagents were purchased from Sigma-Aldrich and used without further purification. $Ru_3(CO)_{12}$ was purchased from Acros Organics, and iodine was purchased from Fisher Scientific. Solvents were purified using an MBraun MB-SP solvent purification system and stored over 4 Å molecular sieves.

^1H and ^{13}C NMR spectra were obtained on either a 300 MHz Mercury or 500 MHz Inova Varian instrument. Peaks were referenced to the residual protons of the deuterated solvents. IR spectra were obtained on a PerkinElmer Spectrum One FT-IR spectrometer using a solution cell equipped with NaCl windows and a path length of 1.0 mm. Thermogravimetric analysis was performed on a TA Instrument Q5000. The samples were ramped from 20 to 600 °C at a rate of 10 °C/min under N_2. Mass spectra were obtained on either an Agilent 6220 TOF mass spectrometer using the DART-TOF mode of operation or a Thermo Scientific DSQ II mass spectrometer using the DIP-NCI/EI-MS mode of operation.

$Ru(CO)_4I_2$. The compound was synthesized using modified literature procedures.[55−57] A solution of $Ru_3(CO)_{12}$ (178.2 mg, 0.2787 mmol) and hexanes (400 mL) was prepared in a 500 mL Schlenk flask. The solution was purged with hexanes saturated with CO for approximately 10 min. The reaction was subsequently irradiated with a blue light-emitting diode (LED) light (450−455 nm, 15 W) while continuing to CO purge for approximately 20 min until the solution turned clear. The solution was then purged with N_2 to remove residual CO present in solution. The solution was cooled to −40 °C using an acetonitrile dry ice cooling bath. A cooled solution of iodine (246.8 mg, 0.9724 mmol) in hexanes (50 mL) was added in one lot to the reaction flask *via* a syringe. A yellowish-brown solid precipitated immediately. The solvent was removed under vacuum and a yellow-orange solid remained. The solid was sublimed at 65 °C at 125 mTorr. Crude yield: 208.7 mg, 53%. Yield after sublimation: 170.1 mg, 44%. The compound was characterized by comparison to literature data.[55,56] IR (hexanes): 2158 (m), 2105 (vs), 2095 (s), and 2066 (s) cm^{-1}.

$Ru(CO)_4Br_2$. The compound was synthesized by a modification of reported literature procedures.[55−57] A three-necked round-bottom flask was equipped with a nitrogen-inlet adapter, a stopper, and a septum. $Ru_3(CO)_{12}$ (300 mg, 0.47 mmol) was measured and added to the flask and then mixed with anhydrous hexanes (500 mL) to create a 6×10^{-4} M $Ru_3(CO)_{12}$ hexane solution. The solution was irradiated by blue LED light (450−455 nm, 15 W) in the presence of carbon monoxide gas, with a vent needle in the septum during this process. The $Ru(CO)_5$ colorless intermediate was formed during photoexcitation of $Ru_3(CO)_{12}$ with the blue LED light. After the reaction mixture had become colorless, the blue LED light was turned off and the CO gas input was stopped. The reaction mixture was purged with N_2 gas for 10 min to make sure no CO remained in the reaction flask, while the reaction mixture was cooled to −40 °C using an acetonitrile/dry ice bath. Bromine (2.9 mL, 1.4 mmol) was dissolved in anhydrous hexanes to produce a dilute bromine solution with a concentration of 0.488 M. Under air-free conditions, the Br_2 hexane solution was injected into the cold $Ru(CO)_5$ solution. The colorless hexane solution turned light yellow and *cis*-$Ru(CO)_4Br_2$ precipitated out as a pale-yellow powder (380 mg, 72%). Most of the hexanes were removed by cannula transfer and then the rest of the hexanes were removed under vacuum. IR (CCl_4): ν_{CO} 2176, 2123, 2105, and 2072 cm^{-1}. The product sublimed as pale-yellow particles at 38 ± 0.5 °C under 125 mTorr with the chiller at 11 °C. The product was crystallized by dissolving the crude *cis*-$Ru(CO)_4Br_2$ in dichloromethane and then slowly adding heptane in the same vial. Crystals were formed overnight under room temperature.

Gas-Phase Measurements. The gas-phase DEA experiments were carried out at the University of Iceland using a crossed-beam instrument, which has been described in detail previously.[33] Here, only a brief description of the experiments will be given. The instrument is under high vacuum, with a base pressure of roughly $7-8 \times 10^{-9}$ Torr. $Ru(CO)_4I_2$ is heated to approximately 50−60 °C and sublimed into the chamber through a capillary to create an effusive molecular beam in the reaction zone. Details on the inlet systems have been published previously.[48] During experiments, the pressure was kept constant at approximately $2-4 \times 10^{-7}$ Torr as monitored with an ion gauge placed at some distance from the reaction zone. The molecular beam is crossed by a well-defined, monochromatic electron beam generated using a trochoidal electron monochromator (TEM). The electron energy was calibrated with reference to the well-established 0 eV resonance for SF_6^- from SF_6 and the energy resolution was estimated from the full width at half-maximum (FWHM) of the SF_6^- ion yield.[58] The electron energy resolution in the present experiments was 110−120 meV. The temperature of the TEM was kept at 120 °C by two halogen lamps in order to prevent deposition of the target compound on the components of the electronic lens system. The ions generated in the reaction zone were analyzed with a commercial HIDEN Epic 1000 quadrupole mass spectrometer (QMS). Mass spectra were recorded by scanning through the relevant mass range at a fixed electron impact energy while ion yield curves were recorded by scanning through the electron energy at fixed mass.

Gas-phase DI spectra were obtained at the University of Florida, using a Thermo Scientific DSQ II with electron impact ionization (70 eV) with an ion source temperature of 100 °C. Samples were introduced using a direct insertion probe (DIP). The tip of a stainless-steel GC-style 10 μL syringe was used to transfer some of the dry samples to the DIP vial. The probe ran the following temperature program: 30−300 °C at a ramp rate of 30 °C/min and hold 1 min at 300 °C.

Surface Science Studies. Surface science experiments were performed at Johns Hopkins University in an UHV chamber equipped with an XPS, QMS, electron flood gun, and ion gun described in more detail elsewhere.[21,59,60] The UHV chamber has a base pressure below 4×10^{-9} Torr. The compound was placed in a reservoir, which was attached to the UHV chamber *via* a leak valve. The compound was heated to 35−40 °C and introduced into the UHV chamber, wherein it adsorbed onto a cooled gold substrate (≈−100 °C) and formed thin films of approximately 1.3−1.9 nm thickness, as measured by XPS.

https://dx.doi.org/10.1021/acs.jpcc.0c01801
J. Phys. Chem. C 2020, 124, 10593−10604

XPS was performed *in situ* with a PHI 5400 using a Mg Kα X-ray anode. Spectra were calibrated to the substrate Au $4f_{7/2}$ peak (BE = 84.0 eV)[61] and processed using commercially available software (CasaXPS). Mass spectrometry performed during surface science experiments used a Balzers Prisma QMS.

The electron source used during all surface science experiments was a commercial flood gun (Specs FG 15/40). The energy of the flood gun was +480 eV and a +20 V bias was applied to the substrate during electron irradiation, producing an incident electron energy throughout all surface science experiments of +500 eV. The bias was used to ensure that all SEs generated during electron irradiation remained on the substrate. A target current of 5 μA was maintained throughout all electron irradiation experiments. The electron dose is reported in terms of both mC/cm^2 and e$^-$/cm^2; 1×10^{16} e$^-$/cm^2 = 1.6 mC/cm^2.

Deposition Studies. Deposits were made at Johns Hopkins University by performing EBID using an Auger spectrometer (PHI 15-155) on silicon substrates with both $Ru(CO)_4I_2$ and its brominated analogue $Ru(CO)_4Br_2$ as precursors. The Auger spectrometer is housed in a UHV chamber (base pressure ~3−4 × 10^{-9} Torr) equipped with a QMS (Stanford Research Systems—200). The compound was heated to about 78 °C and introduced into the chamber *via* a UHV-compatible leak valve equipped with a directional doser used to improve the partial pressure of $Ru(CO)_4I_2$ at the silicon substrate surface. The EBID experiments were performed under steady-state conditions using the electron gun in the Auger spectrometer, operating at a primary beam energy of 3 kV and an emission current of 2 mA. The silicon substrates were held at room temperature and the system pressure was maintained at approximately 1−2 × 10^{-7} Torr during deposition, which proceeded for 5 h. Imaging and analysis of deposits were performed *ex situ* using a JEOL JSM-IT100 secondary electron microscope (SEM) with a 10 kV primary electron beam (8 nm resolution) and a JEOL-made energy-dispersive X-ray spectroscopy (EDX) unit. The deposit thickness was not quantified, but samples were thick enough to have a minimal silicon substrate signal during EDX measurements with up to a 20 kV primary electron beam.

RESULTS

Gas-Phase Low-Energy Electron Interactions. Figure 1 shows a positive ion mass spectrum of $Ru(CO)_4I_2$ recorded at an incident electron energy of 70 eV (top panel) and a negative ion mass spectrum recorded at 0 eV electron energy (bottom panel). Figure 2 shows the negative ion yield curves observed in DEA to $Ru(CO)_4I_2$ in the electron energy range from about 0 to 7 eV, normalized to the pressure of $Ru(CO)_4I_2$. The negative ion yields were measured up to 15 eV, but because no resonances were observed above 7 eV, only the low-energy range is shown.

Negative ion fragments are observed at m/z = 440, 412, 384, 356, and 127 (Figure 1, bottom), corresponding to the formation of $[M - CO]^-$, $[M - 2CO]^-$, $[M - 3CO]^-$, $[M - 4CO]^-$, and I^-, respectively, where M is the parent molecule. The most intense signal is that of $[M - 2CO]^-$, the formation of which has a relative cross section that is more than an order of magnitude higher than for any of the other fragments (Figure 2). From the negative ion yield curves shown in Figure 2, it is apparent that the fragments $[M - CO]^-$, $[M - 2CO]^-$, and I^- all appear through a narrow contribution peaking at 0

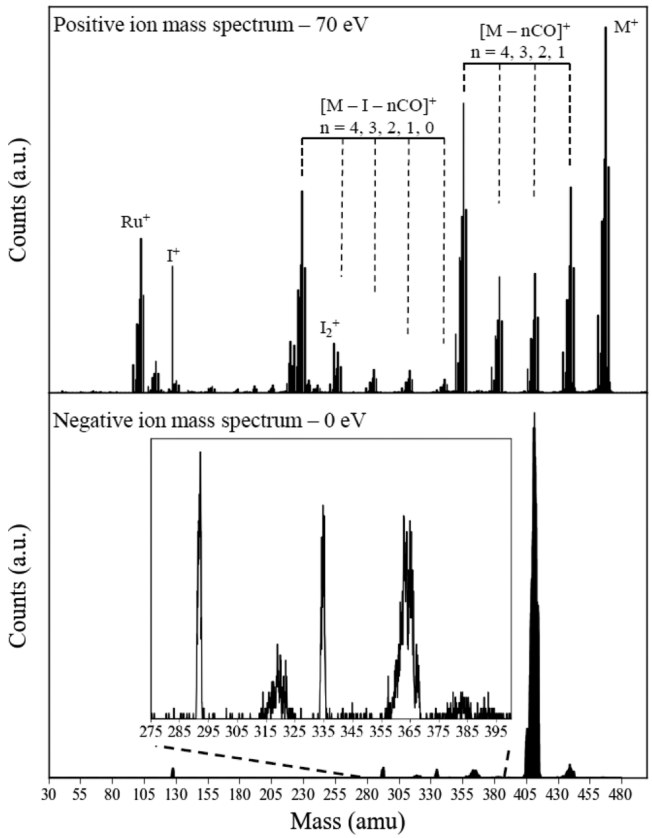

Figure 1. Mass spectra of $Ru(CO)_4I_2$: (Top) positive ion fragments formed at 70 eV incident electron energy due to DI. There is overlap between the I_2^+ (254 amu) peak and the $[M - I - 3CO]^+$ peak envelope (257 amu) from the isotope distribution of ruthenium. (Bottom) Negative ion fragments formed at 0 eV incident electron energy due to DEA. The small peaks at roughly 292, 320, 334, and 364 amu do not correspond to any combination of the components of the parent molecules and are likely impurities left over from a previous experiment.

eV. This requires that all of these DEA processes are exothermic. We attribute all of these contributions to the same low-lying resonance, which is likely associated with the anionic ground state. The $[M - 3CO]^-$ contribution, which peaks at about 0.5 eV, probably originates from the high energy tail of the same resonance shifted because of the higher thermochemical threshold for this process. The DEA ion yield curve for the RuI_2 anion, $[M - 4CO]^-$, is also shown at the bottom of Figure 2. The formation of this fragment through DEA is negligible, although a very small contribution may be anticipated around 4 to 5 eV.

The positive ion mass spectrum (Figure 1, top panel) shows that DI produces much richer fragmentation than observed in DEA. Along with a significant contribution from the parent cation at m/z = 468, prominent fragments are observed at m/z = 440, 412, 384, 356, 254, 229, 127, and 101. These correspond to the carbonyl loss progression $[M - CO]^+$, $[M - 2CO]^+$, $[M - 3CO]^+$, and $[M - 4CO]^+$ and to the ions I_2^+, $[M - 4CO - I]^+$, I^+, and Ru^+, respectively. Minor contributions from m/z = 341, 313, 285, and 257 are also observed, corresponding to loss of one I ligand along with sequential carbonyl loss ($[M - nCO - I]^+$; n = 0−3).

Table 1 lists the relative contributions of individual fragments obtained through DEA and DI to $Ru(CO)_4I_2$ and

https://dx.doi.org/10.1021/acs.jpcc.0c01801
J. Phys. Chem. C 2020, 124, 10593−10604

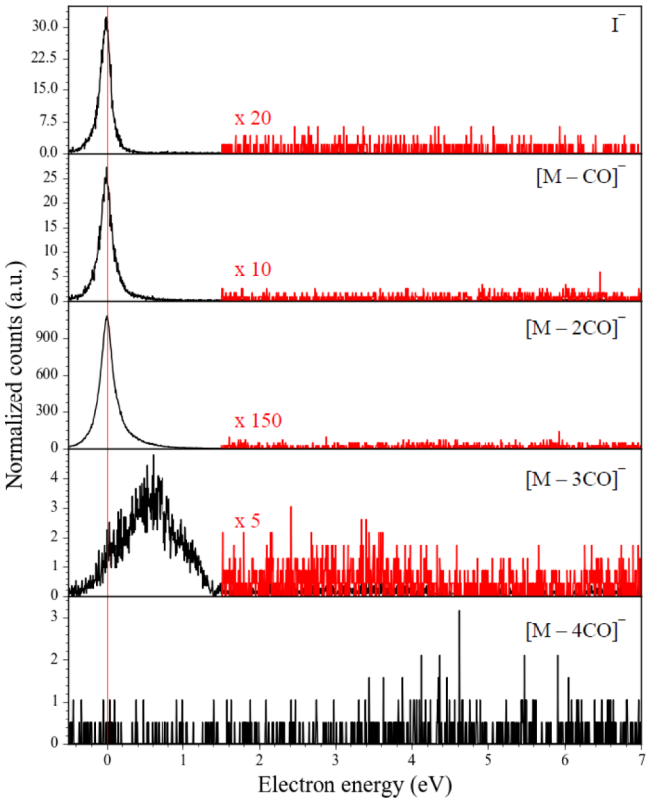

Figure 2. Pressure-normalized negative ion yields from DEA to gas-phase $Ru(CO)_4I_2$ from −0.5 to 7 eV. The solid black lines shows the yield of each fragment detected above the noise. The red lines show magnifications of the high-energy region.

the average CO and I loss per DEA and DI incident, respectively. The relative DEA contributions were found by integrating the negative ion yield from −0.5 to 7.0 eV for each fragment (Figure 2) and dividing that by the total negative ion yield within that energy range. For DI, the relative contributions of the observed fragments were found by integrating over the isotope distribution for each Ru-containing fragment in the positive ion mass spectrum and dividing that by the total positive ion yield of Ru-containing fragments. The relative contributions of each observed fragment listed in Table 1 are normalized to the $[Ru(CO)_2I_2]^{+/-}$ peak intensities, which are set at 100 for both the negative and positive ions. The average CO and I loss per incident for each process were calculated by taking the sum of the relative contribution for each Ru-containing fragment multiplied by the number of CO or I ligands lost and dividing that by the sum of the relative contributions of all Ru-containing fragments. Based on this analysis, DEA produces an average CO loss per incident of 2 and DI produces an average CO loss of 2.8. The average I loss is negligible in DEA (corresponding only to I^- formation) but is close to 0.5 in DI.

Electron Irradiation of $Ru(CO)_4I_2$ Thin Films. Figure 3 shows the evolution of the Ru(3d)/C(1s), O(1s), and $I(3d_{5/2})$

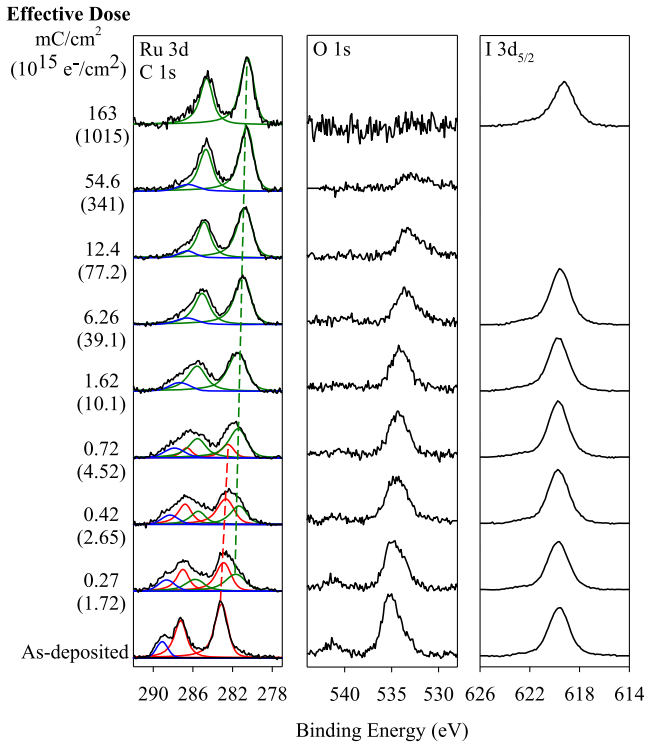

Figure 3. Evolution of the C(1s)/Ru(3d), O(1s), and $I(3d_{5/2})$ XPS regions of ≈1.3−1.9 nm $Ru(CO)_4I_2$ films upon irradiation with 500 eV electrons. The bottom spectrum represents the as-deposited, unirradiated film. Speciation is shown in the C(1s)/Ru(3d) region, where the blue line represents C(1s), the red lines represent the Ru(3d) peaks associated with the $Ru(CO)_4I_2$ compound, and the green lines represent the Ru(3d) peaks associated with the species produced by electron irradiation. The dashed red and green lines in this region show the change in binding energy of these peaks during electron irradiation. The electron dose is shown on the left-hand side in units of mC/cm^2 and, in parentheses, 10^{15} e^-/cm^2.

XPS regions of 1.3−1.9 nm thin films of adsorbed $Ru(CO)_4I_2$ upon irradiation with 500 eV electrons. X-ray sensitivity control studies (Figure S1) were performed in order to

Table 1. Relative Yields of Ru-Containing Ions Produced by Gas-Phase DEA and DI of $Ru(CO)_4I_2$ and Average CO and I Loss per DEA and DI Incident

fragment	chemical formula	*m/z*	relative DEA yield	relative DI yield
$[M - 4CO - 2I]^{+/-}$	Ru	101		203 ± 10
$[M - 4CO - I]^{+/-}$	RuI	229		266 ± 15
$[M - 4CO]^{+/-}$	RuI_2	356	0.04 ± 0.01	352 ± 5
$[M - 3CO]^{+/-}$	$Ru(CO)I_2$	384	1.2 ± 0.1	90 ± 5
$[M-2CO]^{+/-}$	$Ru(CO)_2I_2$	412	100	100
$[M-CO]^{+/-}$	$Ru(CO)_3I_2$	440	2.2 ± 0.3	133 ± 4
$M^{+/-}$	$Ru(CO)_4I_2$	468		249 ± 2
average CO loss			1.99 ± 0.12	2.8 ± 0.2
average I loss			0	0.48 ± 0.07

https://dx.doi.org/10.1021/acs.jpcc.0c01801
J. Phys. Chem. C 2020, 124, 10593−10604

determine the impact of X-ray exposure on the adsorbed $Ru(CO)_4I_2$ thin films. The effect of X-ray irradiation was found to be similar to that of electron irradiation (albeit at a much slower rate), likely due to the SEs generated by the interactions between the X-ray beam and the surface. Based on a comparison of Figures 3 and S1, we estimate that each set of XPS scans delivers an equivalent electron dose of 0.12 mC/cm^2 (0.78×10^{15} e$^-$/cm^2); all XPS figures and data have been adjusted to reflect this comparatively small "additional" electron dose imparted by X-ray irradiation.

The bottom spectra in Figure 3 show the as-deposited, unirradiated $Ru(CO)_4I_2$ film. Upon adsorption, the Ru(3d)/C(1s) region is characterized by three peaks: a doublet with peaks at approximately 283.1 and 287.2 eV, respectively, corresponding to the $Ru(3d_{5/2})$ and $Ru(3d_{3/2})$ transitions[45,62] and a peak at approximately 289.1 eV corresponding to the CO C(1s).[45,62] A low intensity peak centered at approximately 294.3 eV corresponding to the CO C(1s) $\pi-\pi^*$ transition is observed but not shown because of its low intensity. The $Ru(3d_{5/2})$ and $Ru(3d_{3/2})$ transitions are fit as solid red curves, while the CO C(1s) peak is fit by a solid blue curve. The $Ru(3d_{5/2})$ peak position at 283.1 eV is similar to previously reported ruthenium halide species.[45,63] The O(1s) region is initially characterized by a main peak at approximately 535.2 eV and a lower intensity peak centered at 541.3 eV corresponding to the CO O(1s) $\pi-\pi^*$ transition, which is typical for adsorbed CO species.[45,62] Finally, the unirradiated $I(3d_{5/2})$ region is characterized by a single, symmetric peak at approximately 619.6 eV.

Upon electron irradiation, the C(1s)/Ru(3d) region broadens considerably to lower binding energies. The resultant spectral envelope can be fit by a combination of a C(1s) peak along with two sets of $Ru(3d_{5/2})/(3d_{3/2})$ doublets. One of these doublets has peak positions corresponding to those of the parent compound (solid red curves), while the other doublet, associated with a species produced by electron irradiation, has $Ru(3d_{5/2})/(3d_{3/2})$ peaks at approximately 281.5 and 285.7 eV, respectively (solid green curves). As the electron dose increases, the contribution of the $Ru(3d_{5/2})/(3d_{3/2})$ doublet associated with the parent compound decreases steadily. After an electron dose of 1.6 mC/cm^2 (10.1×10^{15} e$^-$/cm^2), none of the parent $Ru(CO)_4I_2$ species remains. Over this same range of electron doses, the intensity of the $Ru(3d_{5/2})/(3d_{3/2})$ doublet associated with the electron-irradiated species increases, while its peak binding energies decrease slightly with increasing electron dose. After an electron dose of 1.6 mC/cm^2 (10.1×10^{15} e$^-$/cm^2), the Ru(3d)/C(1s) region can be well-fit by a single $Ru(3d_{5/2})/Ru(3d_{3/2})$ doublet with peaks at approximately 280.4 and 284.6 eV along with a C(1s) peak. For electron doses >1.6 mC/cm^2 (10.1×10^{15} e$^-$/cm^2), the Ru(3d) peak profile remains unchanged. Despite the change in Ru speciation, there is no change in the coverage of ruthenium atoms as a result of electron irradiation. In contrast, electron irradiation produces a steady decrease in the intensity of the C(1s) peak over the entire sequence of electron doses, with peak fitting suggesting that no carbon remains after an electron dose of 163 mC/cm^2 (1015×10^{15} e$^-$/cm^2).

Electron irradiation also causes the O(1s) peak to decrease in intensity, as well as broaden and shift to lower binding energy. After an electron dose of 6.2 mC/cm^2 (39.1×10^{15} e$^-$/cm^2), the O(1s) region is characterized by a single broadened peak centered at 533.6 eV, a decrease in binding energy of about 1.6 eV compared to the parent compound. At greater electron doses (>6.2 mC/cm^2, 39.1×10^{15} e$^-$/cm^2), the O(1s) peak continues to decrease in intensity, broaden, and shift to lower binding energy, as can be seen in Figure 3. Ultimately, no oxygen is observed after an electron dose of 163 mC/cm^2 (1015×10^{15} e$^-$/cm^2). In contrast to the behavior in the Ru(3d)/C(1s) and O(1s) regions, the $I(3d_{5/2})$ region does not change significantly during electron irradiation, indicating an absence of iodine desorption. However, determination of the fate of the Ru−I bond through detailed analysis of the $I(3d_{5/2})$, Ru(3d), and Au(4f) XPS regions is complicated by the similar electronegativities of iodine, ruthenium, and gold (2.66, 2.2, and 2.4, respectively). Consequently, dissociation of the Ru−I bond would not produce any changes in the $I(3d_{5/2})$ or Ru(3d) peak positions; the subsequent formation of a gold iodide also would not change the $I(3d_{5/2})$ or Au(4f) peak positions. However, a previous study of electron-induced decomposition of $Pt(CO)_2Cl_2$ revealed that the chloride ligand did not dissociate from the platinum during the initial stage of electron-induced dissociation;[47] thus, we conclude that the Ru−I bond likely remains intact.

Figure 4 shows the change in the number of carbonyl ligands remaining on the surface, as measured by the O(1s) area, as a function of electron dose. Although both the C(1s) area and the O(1s) area can be used to represent the number of carbonyl ligands remaining on the surface, the O(1s) area was chosen because of the significant overlap between the C(1s) and $Ru(3d_{3/2})$ peaks. Initially, 4 CO ligands are present in the adsorbed molecular $Ru(CO)_4I_2$ species. Upon electron irradiation, the O(1s) area quickly decreases to 50% of its initial value (i.e., loss of an average of 2 CO ligands per parent molecule) after an electron dose of about 6 mC/cm^2 (4×10^{16} e$^-$/cm^2). This initial CO loss regime is highlighted in the inset in Figure 4. Larger electron doses lead to the loss of the remaining 2 CO ligands at a much slower rate, with no CO

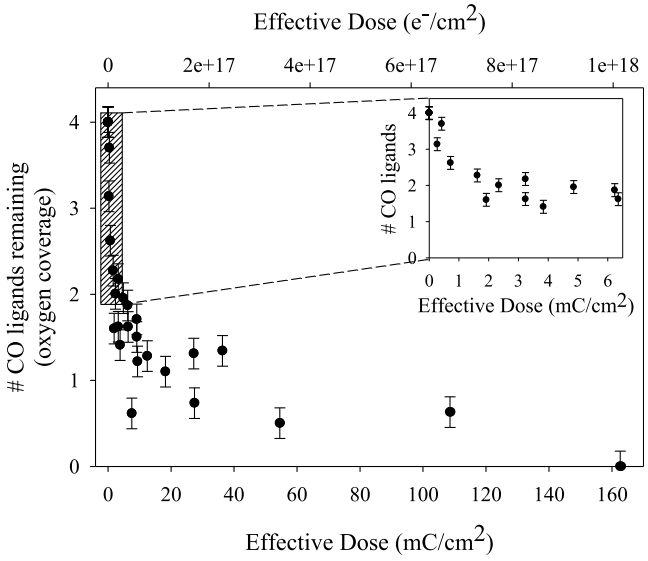

Figure 4. Number of CO ligands remaining (measured by the oxygen coverage) as a function of electron dose, for $Ru(CO)_4I_2$ films exposed to 500 eV electrons. The effective electron dose is expressed in units of mC/cm^2 (main axis) and e$^-$/cm^2 (top axis). The highlighted region shows the CO ligand loss for electron doses <6 mC/cm^2 (4×10^{16} e$^-$/cm^2).

https://dx.doi.org/10.1021/acs.jpcc.0c01801
J. Phys. Chem. C 2020, 124, 10593−10604

ligands remaining after an electron dose of about 160 mC/cm^2 (1×10^{18} e$^-$/cm^2).

The kinetics of electron-stimulated CO desorption during the initial regime of electron exposure (<6 mC/cm^2, 4×10^{16} e$^-$/cm^2) of adsorbed $Ru(CO)_4I_2$ are shown in Figure 5. The inset shows a representative mass spectrum taken during electron exposure, with visible peaks at m/z = 12, 16, and 28 corresponding to C, O, and CO, respectively, similar to previous observations of CO desorbing from thin films of organometallic precursors during irradiation with 500 eV electrons.[34,47] The top graph shows the normalized evolution of gas-phase CO, as observed by mass spectrometry using the C (m/z = 12) peak (solid black line). The C peak at m/z = 12 has good overlap with both the O (m/z = 16) and CO (m/z = 28) peaks, as can be seen in Figure S2 (Supporting Information) and can thus be considered representative of CO desorbing from the surface during electron irradiation. The bottom graph shows the concurrent change in fractional coverage of $Ru(CO)_4I_2$ (dark blue filled circles, left axis) determined by analysis of the Ru(3d) XPS region, overlaid with the number of CO ligands remaining on the surface (inverted light blue triangles, right axis); the latter was determined by the change in the fractional oxygen coverage as measured by the O(1s) peak. Analysis of the top and bottom panels in Figure 5 reveals that the rates of CO desorption and loss of the parent $Ru(CO)_4I_2$, as well as the change in the number of CO ligands in the adsorbate, all follow the same kinetic profile as a function of the electron dose.

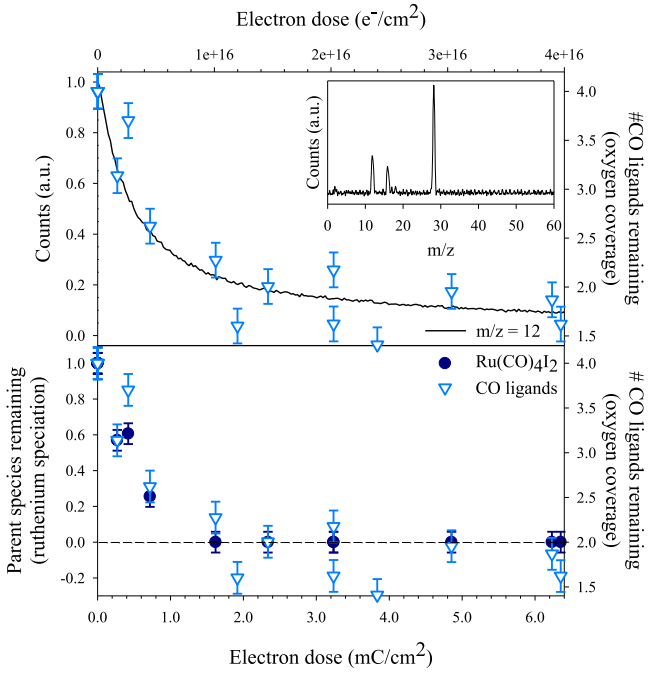

Figure 5. (Top) Kinetics of electron-stimulated gas-phase CO desorption from $Ru(CO)_4I_2$ films upon irradiation with 500 eV electrons as measured *via* mass spectrometry by the normalized C (m/z = 12) peak intensity (solid black line) and the number of CO ligands remaining on the surface (light blue inverted triangles, right axis) as measured by the O(1s) XPS peak area (see Figure 3). The inset shows a representative mass spectrum of volatile species during electron irradiation. (Bottom) The number of CO ligands remaining on the surface (light blue inverted triangles, right axis) overlaid with fractional concentration of the parent species, $Ru(CO)_4I_2$ (dark blue filled circles, left axis), as measured by the Ru(3d) XPS peaks (see Figure 3). The electron dose is expressed in units of mC/cm^2 (main axis) and e$^-$/cm^2 (top axis).

Electron Beam-Induced Deposition. Figure 6 shows representative EDX spectra from deposits made by exposing a silicon substrate to a high-energy (3 kV) electron beam in the presence of gas-phase $Ru(CO)_4I_2$ (top) and the bromide complex $Ru(CO)_4Br_2$ (bottom). The images to the right of each spectrum are SEM images of the respective deposits. The EDX analysis demonstrates that the $Ru(CO)_4I_2$ deposit (top) is composed of Ru (31 at. %), I (56 at. %), C (8 at. %), and O (5 at. %). Analysis of the EDX spectrum from the $Ru(CO)_4Br_2$ deposit (bottom) shows a similar composition of 27 at. % Ru, 54 at. % Br, 15 at. % C, and 4 at. % O. In both deposits, Ru/X (X = Br, I) is close to the 1:2 ratio found in the precursor molecules. Because of overlap between the C EDX peak and some Ru EDX peaks, it is likely that the estimated at. % C is slightly high and that the true carbon-to-oxygen ratio in the deposit is close to 1:1. The average CO/Ru ratio in the deposits is therefore approximately 1:6 − significantly lower than that found in the precursor (4:1). This indicates that the majority of CO ligands associated with the precursor molecule are not incorporated into the deposit. Elemental maps of the Ru L, I L, C K, O K, and Si K X-rays (shown in the Supporting Information, Figure S3) show that all elements associated with the precursor molecule are localized within the deposit.

DISCUSSION

As can be seen in Figures 1 and 2, DEA to gas-phase $Ru(CO)_4I_2$ molecules overwhelmingly leads to the loss of two CO ligands. The loss of a single CO ligand is also observed but with about 40 times less intensity. While significant loss of two CO units is a common observation in DEA to metal carbonyl compounds at low incident energy, it is uncommon for the loss of two CO ligands to be dominant over the loss of a single CO.[26,28,44,64] For this process to proceed at 0 eV incident energy, the electron affinity of the charge-retaining fragment (here, $[Ru(CO)_2I_2]^-$) must exceed the bond dissociation energy (BDE) needed to cleave the two Ru−CO bonds. We note that the extraction time from the ionization region of the instrument used for the DEA measurements is on the order of 10 μs, while the flight time through the QMS is about 50 μs. Therefore, if significant excess energy is retained by the fragment after the first CO loss, loss of a second CO ligand within 10 μs is more likely than the survival of this metastable anion over the approximately 50 μs flight through the QMS. Ru−I bond dissociation is also observed, producing I$^-$, and this pathway is about 30 times less significant than the 2 CO loss pathway (Figures 1 and 2), making it a comparably minor product. Finally, the loss of 3 CO units is observed through the high-energy side of the 0 eV resonance but with relatively low intensity.

This is further rationalized by the well-known *trans* effect in inorganic chemistry. In the neutral precursor, the two carbonyl ligands *trans* to one another will be more weakly bound to the metal center than the two *trans* to the iodide ligands because of π-backbonding, which dominates metal−CO bond strengths. For the carbonyl ligands *trans* to iodide, the iodide lone pairs donate electron density into the metal d orbitals that participate in backbonding with the carbonyl π^* orbitals, strengthening the Ru−CO bonds through increased π-backbonding. Conversely, for the carbonyl ligands *trans* to each

https://dx.doi.org/10.1021/acs.jpcc.0c01801
J. Phys. Chem. C 2020, 124, 10593−10604

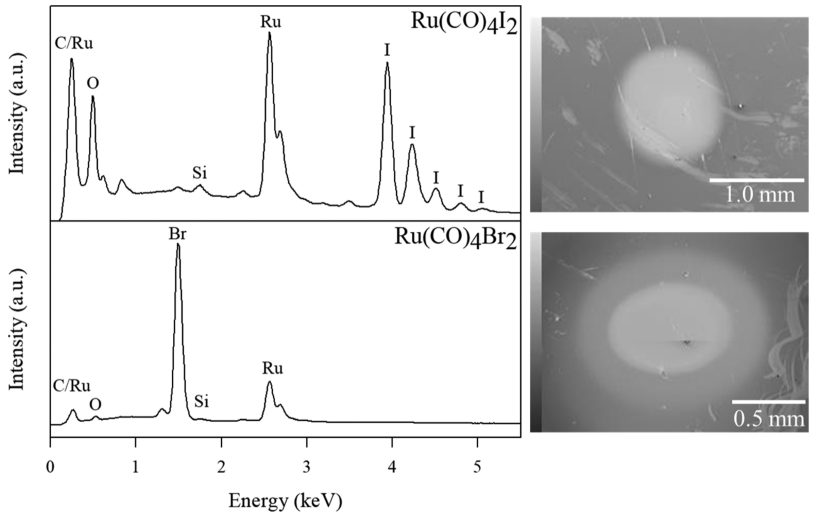

Figure 6. EDX spectra of deposits made by EBID from (top) $Ru(CO)_4I_2$ and (bottom) $Ru(CO)_4Br_2$ under UHV conditions. To the right of each spectrum are SEM images of the respective deposits. Both the EDX spectra and the SEM images were taken using a primary electron beam energy of 10 kV.

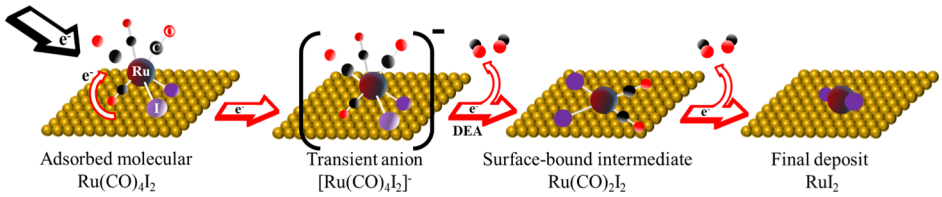

Figure 7. Schematic representation of the electron-induced surface reactions underlying EBID from $Ru(CO)_4I_2$. In the first step, electron attachment to $Ru(CO)_4I_2$ produces a transient negative ion that decomposes through the loss of two carbonyl ligands (DEA). In the second slower step, the residual two carbonyl ligands desorb from the surface under extended electron irradiation.

other, both carbonyl ligands are π-acids that compete for electron density in the same d orbitals, weakening both Ru−CO bonds through the decrease in backbonding. Hence, the sum of the BDEs for the two Ru−CO bonds that are *trans* to one another is the likeliest to be lower than the electron affinity of the corresponding fragment ($[Ru(CO)_2I_2]$), fueling the dominance of this pathway at 0 eV incident electron energy.

Conversely, DI of $Ru(CO)_4I_2$ produces much more extensive fragmentation, with appreciable intensities from the parent cation, fragments resulting from the loss of 1−4 CO ligands, and fragments associated with the loss of both CO and I. Based on the intensity-averaged fragmentation pattern, an average of three CO ligands and 0.5 iodide ligands are lost per DI incident at 70 eV, as seen in Table 1. This can be compared to DEA, where the average CO loss per incident is close to two and the iodide loss is negligible.

Analysis of Figures 3, 4, and 5 indicates that during the initial stage of electron-stimulated decomposition of adsorbed $Ru(CO)_4I_2$ molecules (electron doses <1.6 mC/cm^2, 10.1 × 10^{15} e$^-$/cm^2), an average of about 2 CO ligands per parent molecule desorb from the substrate. The initial step in electron-induced deposition of $Ru(CO)_4I_2$ can thus be described as

$$Ru(CO)_4I_{2(ads)} + e^- \rightarrow Ru(CO)_2I_{2(ads)} + 2CO_{(g)}\uparrow \quad (5)$$

Here, the adsorbed product ($Ru(CO)_2I_{2(ads)}$) is best viewed as a partially decarbonylated intermediate; the molecular formula is intended to be stoichiometric rather than to denote a specific bonding structure. This initial step is illustrated in Figure 7.

Since this initial step corresponds to the decomposition of the parent molecule, it can be compared to the gas-phase electron-induced fragmentation of $Ru(CO)_4I_2$ *via* DEA (Figures 1 and 2) and DI (Figure 2). Similarly to DEA-induced decomposition of $Ru(CO)_4I_2$, the initial electron-induced ligand loss step in electron-induced deposition of $Ru(CO)_4I_2$ proceeds *via* loss of two CO ligands and no iodide loss from the surface is observed. This is in marked contrast with DI-induced fragmentation, which is a statistical process that leads to an average loss of about 3 CO ligands and 0.5 iodide ligands per DI-initiated event. This comparison shows that the extent of the initial fragmentation in the surface experiments is much closer to what is observed in the gas phase for DEA rather than *via* DI.

The initial electron-induced decomposition step is determined by the energy distribution of the SEs and the cross sections for the various possible electron-induced decomposition processes (DEA, DI, ND, and DD) as a function of the electron energy, i.e., the effective damage yield.[19,26,48] The observation that the extent of the electron-induced decomposition of adsorbed $Ru(CO)_4I_2$ matches that which is observed for DEA in the gas phase and is much less extensive than what is observed for DI suggests three possibilities: (i) the SE energy distribution is not significant above the ionization energy of $Ru(CO)_4I_2$, (ii) on the surface, DI of $Ru(CO)_4I_2$ is more efficiently quenched than DEA, or (iii) the absolute cross sections for DI of $Ru(CO)_4I_2$ are lower than those for DEA. Regarding (i), the SE energy distribution from Au surfaces exposed to 300 eV has indeed been shown to be narrow, with the majority of SEs having energies below 10 eV.[65] However,

https://dx.doi.org/10.1021/acs.jpcc.0c01801
J. Phys. Chem. C 2020, 124, 10593−10604

this energy distribution is sensitive to surface contamination and topography.[65] In this regard, previous studies have shown no significant difference in the products formed when organometallic precursors adsorbed on different surfaces likely to have different SE distributions (principally Au and HOPG) have undergone electron-stimulated reactions/decomposition.[34,40,45,68] The second possibility (ii) has been recently discussed in the context of $Pt(CO)_2Cl_2$,[48] wherein the metastable nature of DI may cause it to be effectively quenched at surfaces after the initial loss of the most loosely bound ligands.[47] This may also be the case for $Ru(CO)_4I_2$, where the two CO ligands *trans* to the iodide ligands are more strongly bound than the other CO ligands. However, the gas-phase DI spectrum of $Ru(CO)_4I_2$ shows no suggestion of any particular stability associated with $[Ru(CO)_2I_2]^+$, making this explanation unlikely, although additional stabilization may be provided by the surface. With regard to (iii), we find the pressure-normalized count rates for all DEA fragments and all DI fragments to be similar (within the same order of magnitude) when the DEA count rates are normalized with respect to the well-established absolute cross section for SF_6^- from SF_6 at 0 eV[58] and the DI count rates with respect to the absolute cross section for Ar^+ from Ar at 70 eV.[67] However, DEA is a resonant process and proceeds within a narrow energy range, while DI is nonresonant and thus is efficient over a very broad energy range above its threshold. Thus, if we integrate the cross section over the entire energy range, the cross section for DI will be significantly higher than that of DEA. The SE energy distribution (i) will therefore also have a determinative effect on the integral damage yield.[19,26,48] Finally, we note that ND was not studied here, and recent studies have suggested that it may play a role in FEBID.[64,68,69]

Nonetheless, our experimental evidence shows a clear correlation between the predictions from gas-phase DEA and the initial electron-induced decomposition of adsorbed $Ru(CO)_4I_2$, consistent with DEA, rather than DI, as the primary route for the initial electron-induced decomposition step of this molecule. Further, independent of the potential contribution from ND, it is clear from the current data that DI is significantly less efficient for electron-induced decomposition of $Ru(CO)_4I_2$ on the surface than in the gas phase as DI leads to significantly more fragmentation of $Ru(CO)_4I_2$ in the gas phase than is observed on the surface, while this is not the case for DEA.

The second electron-induced reaction stage of adsorbed $Ru(CO)_4I_2$ proceeds at higher electron doses (>1.6 mC/cm^2, 10.1×10^{15} e$^-$/cm^2). In this regime, the remaining carbon and oxygen are removed from the surface, seen most clearly by the absence of any oxygen after an electron dose of 163 mC/cm^2 (1015×10^{15} e$^-$/cm^2, Figures 3 and 4). This second step can therefore be described as

$$Ru(CO)_2I_{2(ads)} + e^- \rightarrow RuI_{2(ads)} + 2CO_{(g)}\uparrow \quad (6)$$

This second step, shown schematically in Figure 7, differs from several previous studies of electron-induced deposition of adsorbed carbonyl-containing organometallic precursor molecules, including $Co(CO)_3NO$, $W(CO)_6$, $CpFe(CO)_2Mn(CO)_5$, and $CpFe(CO)_2Re(CO)_5$.[34,40,43,70] For these compounds, the initial electron-initiated precursor decomposition step leads to multiple CO ligand loss, analogous to $Ru(CO)_4I_2$ (eq 5, Figure 7), but continued electron irradiation decomposed the remaining CO ligands into graphitic carbon and reactive oxygen species, which then oxidized the metal atoms. Conversely, in electron-induced deposition studies of adsorbed $H_2FeRu_3(CO)_{12}$, $(\eta^3\text{-}C_3H_5)Ru(CO)_3Br$, and $Pt(CO)_2Cl_2$, no CO decomposition is observed.[45,47,51] Because the fate of the CO ligands (i.e., desorption or decomposition) plays an important role in determining the ultimate metal content of FEBID nanostructures, it is useful to consider the potential underlying causes of electron-induced CO decomposition ($CO_{(ads)} + e^- \rightarrow C_{(ads)} + ROS$) *versus* desorption ($CO_{(ads)} + e^- \rightarrow CO_{(g)}$) in the partially decarbonylated intermediates, which are common intermediates in FEBID of metal carbonyls.

Several factors may influence electron-induced CO decomposition *versus* desorption in these partially decarbonylated organometallic intermediates, including the oxophilicities of the various metal centers (Co, W, Fe, Mn, Re, Ru, and Pt) and the nature of the ancillary ligands [($\eta^3\text{-}C_3H_5$), NO, Cl, Br, and I]. Analysis of the oxophilicities of the oxidized metal centers in the compounds that undergo electron-induced CO decomposition (Co, W, Mn, Fe, and Re) *versus* desorption (Fe, Ru, and Pt) does not show a strong correlation between oxophilicity and decomposition *versus* desorption (the aforementioned metals have oxophilicities of 0.4, 0.8, 0.4, 0.4, and 0.5, respectively, *vs* 0.4, 0.4, and 0.1, respectively).[71] However, it is evident that metal-halide bonds are present in most of the precursors that undergo electron-induced CO desorption rather than decomposition, and none of the precursors that undergo electron-induced CO decomposition contain halide ligands. This suggests that the presence of halides promotes electron-induced CO desorption from partially decarbonylated intermediates.

Electron beam-induced deposits created from $Ru(CO)_4I_2$ under a constant partial pressure of precursor molecules and a constant electron emission current (Figure 6) are composed primarily of ruthenium and iodine, with a ≈2:1 iodine-to-ruthenium ratio and minimal (<10 at. %) carbon and oxygen contamination. In related studies, we have shown that the CO ligands in the partially decarbonylated $Ru(CO)_2I_2$ intermediate are stable at room temperature (see Figure S4). As a result, all of the elementary reaction steps responsible for the formation of the deposit in FEBID should be electron-induced rather than thermal processes. Under these conditions, the observation that the composition of the EBID structures in Figure 6 coincides with the prediction of the low-temperature UHV electron irradiation studies in the limit of larger electron doses supports the relevance of the two deposition steps identified by the gas phase and surface studies (eqs 5 and 6) to FEBID. Deposits formed from $Ru(CO)_4Br_2$ show similar results, suggesting that these electron-induced processes are independent of the nature of the halogen, as was previously found for $Pt(CO)_2X_2$ and $(\eta^3\text{-}C_3H_5)Ru(CO)_3X$ (X = Br, Cl). Although the persistence of the iodide ligand in the deposit presents a limitation to the metal purity of deposits made from this precursor, previous studies have shown that residual halide ligands may be removable by exposure to atomic hydrogen (e.g., $Pt(NH_3)_2Cl_2$, $Pt(CO)_2Cl_2$)[54,72] while residual carbon contamination is much harder to remove.

The presence of small quantities of carbon and oxygen in these deposits in roughly equal concentrations may be due to the relatively slow rate of the second deposition step (eq 6), causing some residual CO ligands to be trapped in the growing deposit. A comparison of the relative rates of the two electron-induced ligand dissociation steps shows that the first step (eq 5) requires an electron dose of approximately 1.6 mC/cm^2

https://dx.doi.org/10.1021/acs.jpcc.0c01801
J. Phys. Chem. C 2020, 124, 10593−10604

(10.1×10^{15} e^-/cm^2), while the second step (eq 6) is a slower process requiring an electron dose of about 163 mC/cm^2 (1015×10^{15} e^-/cm^2). Electron-induced M−CO bond dissociation of the partially decarbonylated intermediate ($Ru(CO)_2I_2$, eq 6) is therefore about 2 orders of magnitude slower than the initial electron-induced carbonyl loss step (eq 5). Under these circumstances, some residual CO ligands in the partially decarbonylated intermediate may be unable to desorb (eq 6) before the steady-state film growth causes the electron intensity experienced by the partially decarbonylated intermediates to fall to zero, thus preventing further CO desorption and producing this contamination. Another potential source of carbon and oxygen contamination may be the trapping of desorbing CO within the growing deposit lattice such that it recombines before escaping.

CONCLUSIONS

A comprehensive study has been performed on the electron-induced reactions of $Ru(CO)_4I_2$ in the gas phase, adsorbed on surfaces, and in EBID. In the gas phase, DEA to $Ru(CO)_4I_2$ was found to overwhelmingly lead to loss of two carbonyl ligands *via* a resonance centered close to 0 eV, while DI of $Ru(CO)_4I_2$ was found to produce much more extensive fragmentation. Surface science studies of thin films of $Ru(CO)_4I_2$ under UHV conditions found that 500 eV electron irradiation caused an initial deposition step characterized by loss of two carbonyl ligands, forming a partially decarbonylated intermediate, followed by a 2 orders of magnitude slower second step characterized by the loss of the remaining two carbonyl ligands. A comparison of the gas-phase and surface science data shows that the extent of the initial electron-induced reaction of adsorbed $Ru(CO)_4I_2$ matches the ligand loss observed for DEA in the gas phase, while it is much less extensive than the fragmentation observed for DI in the gas phase. This may be due to the overlap of the SE energy distribution with the energy dependence of the DEA and DI cross sections or due to more effective quenching of DI as compared to DEA on the surface. Interestingly, the residual carbonyl ligands in the partially decarbonylated intermediate desorb from the surface under sustained electron irradiation, rather than decomposing and being incorporated into the deposit as has been observed for other metal carbonyls. Consistent with the predictions of the surface science studies, deposition of $Ru(CO)_4I_2$ and its bromide derivative $Ru(CO)_4Br_2$ with a 3 kV focused electron beam produced deposits with a ≈1:2 ruthenium-to-halide ratio and minimal carbon and oxygen contamination. Coupled with previous studies of similar halogenated metal carbonyl precursors (i.e., $Pt(CO)_2Cl_2$ and $Pt(CO)_2Br_2$), these results support the idea that organometallic precursors with carbonyl and halide ligands can produce nanostructures using FEBID free of carbon or oxygen contamination.

ASSOCIATED CONTENT

Supporting Information

The Supporting Information is available free of charge at https://pubs.acs.org/doi/10.1021/acs.jpcc.0c01801.

X-ray sensitivity control; kinetic trace of m/z = 28, 16, and 12 during electron irradiation; elemental maps of the deposit; XPS of electron irradiation + heating to room temperature (showing thermal stability of residual CO ligands); and mass spectrum for $Ru(CO)_4Br_2$ (PDF)

AUTHOR INFORMATION

Corresponding Author

D. Howard Fairbrother − *Department of Chemistry, Johns Hopkins University, Baltimore, Maryland 21218-2685, United States;* orcid.org/0000-0003-4405-9728; Email: howardf@jhu.edu

Authors

Rachel M. Thorman − *Department of Chemistry, Johns Hopkins University, Baltimore, Maryland 21218-2685, United States*

Pernille A. Jensen − *Department of Chemistry and Science Institute, University of Iceland, 107 Reykjavik, Iceland*

Jo-Chi Yu − *Department of Chemistry, University of Florida, Gainesville, Florida 32611-7200, United States*

Scott J. Matsuda − *Department of Chemistry, University of Florida, Gainesville, Florida 32611-7200, United States*

Lisa McElwee-White − *Department of Chemistry, University of Florida, Gainesville, Florida 32611-7200, United States;* orcid.org/0000-0001-5791-5146

Oddur Ingólfsson − *Department of Chemistry and Science Institute, University of Iceland, 107 Reykjavik, Iceland;* orcid.org/0000-0002-7100-9438

Complete contact information is available at: https://pubs.acs.org/10.1021/acs.jpcc.0c01801

Author Contributions

‖R.M.T. and P.A.J. equally contributed to this work.

Notes

The authors declare no competing financial interest.

ACKNOWLEDGMENTS

L.M.W. and D.H.F. thank the National Science Foundation for support of this work through the linked collaborative grants CHE-1607621, CHE-1904559, CHE-1607547, and CHE-1904802. Support of mass spectrometry instrumentation at the University of Florida was provided by the National Institutes of Health through the grant S10 OD021758-01A1. OI acknowledges support from the Icelandic Center of Research (RANNIS), grant no. 13049305(1−3), and the University of Iceland Research Fund. This work was conducted within the framework of ELENA, a European Union's Horizon 2020 research and innovation program under the Marie Skłodowska-Curie grant agreement no. 722149.

REFERENCES

(1) Chattopadhyay, S.; Chen, L.-C.; Chen, K.-H. Nanotips: Growth, Model, and Applications. *Crit. Rev. Solid State Mater. Sci.* **2006**, *31*, 15−53.

(2) Utke, I.; Hoffmann, P.; Melngailis, J. Gas-Assisted Focused Electron Beam and Ion Beam Processing and Fabrication. *J. Vac. Sci. Technol., B: Microelectron. Nanometer Struct.–Process., Meas., Phenom.* **2008**, *26*, 1197.

(3) van Dorp, W. F.; Hagen, C. W. A Critical Literature Review of Focused Electron Beam Induced Deposition. *J. Appl. Phys.* **2008**, *104*, 081301.

(4) Huth, M.; Porrati, F.; Schwalb, C.; Winhold, M.; Sachser, R.; Dukic, M.; Adams, J.; Fantner, G. Focused Electron Beam Induced Deposition: A Perspective. *Beilstein J. Nanotechnol.* **2012**, *3*, 597−619.

(5) van Dorp, W. F.; van Someren, B.; Hagen, C. W.; Kruit, P.; Crozier, P. A. Approaching the Resolution Limit of Nanometer-Scale Electron Beam-Induced Deposition. *Nano Lett.* **2005**, *5*, 1303−1307.
(6) George, H. C.; Orlova, T. A.; Orlov, A. O.; Snider, G. L. Novel Method for Fabrication of Nanoscale Single-Electron Transistors: Electron Beam Induced Deposition of Pt and Atomic Layer Deposition of Tunnel Barriers. *J. Vac. Sci. Technol., B: Nanotechnol. Microelectron.: Mater., Process., Meas., Phenom.* **2011**, *29*, 06FB01.
(7) Pablo-Navarro, J.; Sanz-Hernández, D.; Magén, C.; Fernández-Pacheco, A.; de Teresa, J. M. Tuning Shape, Composition and Magnetization of 3D Cobalt Nanowires Grown by Focused Electron Beam Induced Deposition (FEBID). *J. Phys. D: Appl. Phys.* **2017**, *50*, 18LT01.
(8) Keller, L.; Al Mamoori, M. K. I.; Pieper, J.; Gspan, C.; Stockem, I.; Schröder, C.; Barth, S.; Winkler, R.; Plank, H.; Pohlit, M.; et al. Direct-Write of Free-Form Building Blocks for Artificial Magnetic 3D Lattices. *Sci. Rep.* **2018**, *8*, 6160.
(9) Winkler, R.; Schmidt, F.-P.; Haselmann, U.; Fowlkes, J. D.; Lewis, B. B.; Kothleitner, G.; Rack, P. D.; Plank, H. Direct-Write 3D Nanoprinting of Plasmonic Structures. *ACS Appl. Mater. Interfaces* **2017**, *9*, 8233−8240.
(10) Höflich, K.; Yang, R. B.; Berger, A.; Leuchs, G.; Christiansen, S. The Direct Writing of Plasmonic Gold Nanostructures by Electron-Beam-Induced Deposition. *Adv. Mater.* **2011**, *23*, 2657−2661.
(11) Sengupta, S.; Li, C.; Baumier, C.; Kasumov, A.; Guéron, S.; Bouchiat, H.; Fortuna, F. Superconducting Nanowires by Electron-Beam-Induced Deposition. *Appl. Phys. Lett.* **2015**, *106*, 042601.
(12) Córdoba, R.; Ibarra, A.; Mailly, D.; De Teresa, J. M. Vertical Growth of Superconducting Crystalline Hollow Nanowires by He^+ Focused Ion Beam Induced Deposition. *Nano Lett.* **2018**, *18*, 1379−1386.
(13) Gabureac, M.; Bernau, L.; Utke, I.; Boero, G. Granular Co−C Nano-Hall Sensors by Focused-Beam-Induced Deposition. *Nanotechnology* **2010**, *21*, 115503.
(14) Arnold, G.; Winkler, R.; Stermitz, M.; Orthacker, A.; Noh, J. H.; Fowlkes, J. D.; Kothleitner, G.; Huth, M.; Rack, P. D.; Plank, H. Tunable 3D Nanoresonators for Gas-Sensing Applications. *Adv. Funct. Mater.* **2018**, *28*, 1707387.
(15) Schwalb, C. H.; Grimm, C.; Baranowski, M.; Sachser, R.; Porrati, F.; Reith, H.; Das, P.; Müller, J.; Völklein, F.; Kaya, A.; et al. A Tunable Strain Sensor Using Nanogranular Metals. *Sensors* **2010**, *10*, 9847−9856.
(16) Utke, I.; Hoffmann, P.; Berger, R.; Scandella, L. High-Resolution Magnetic Co Supertips Grown by a Focused Electron Beam. *Appl. Phys. Lett.* **2002**, *80*, 4792−4794.
(17) Edinger, K.; Becht, H.; Becker, R.; Bert, V.; Boegli, V. A.; Budach, M.; Göhde, S.; Guyot, J.; Hofmann, T.; Hoinkis, O.; et al. A Novel Electron-Beam-Based Photomask Repair Tool. In *23rd Annual BACUS Symposium on Photomask Technology*; Kimmel, K. R., Staud, W., Eds.; International Society for Optics and Photonics, 2003; Vol. *5256*, p 1222.
(18) Bret, T.; Hofmann, T.; Edinger, K. Industrial Perspective on Focused Electron Beam-Induced Processes. *Appl. Phys. A* **2014**, *117*, 1607−1614.
(19) Thorman, R. M.; T.P., R. K..; Fairbrother, D. H.; Ingólfsson, O. The Role of Low-Energy Electrons in Focused Electron Beam Induced Deposition: Four Case Studies of Representative Precursors. *Beilstein J. Nanotechnol.* **2015**, *6*, 1904−1926.
(20) Engmann, S.; Stano, M.; Matejčík, Š.; Ingólfsson, O. Gas Phase Low Energy Electron Induced Decomposition of the Focused Electron Beam Induced Deposition (FEBID) Precursor Trimethyl (Methylcyclopentadienyl) Platinum(IV) ($MeCpPtMe_3$). *Phys. Chem. Chem. Phys.* **2012**, *14*, 14611−14618.
(21) Wnuk, J. D.; Gorham, J. M.; Rosenberg, S. G.; van Dorp, W. F.; Madey, T. E.; Hagen, C. W.; Fairbrother, D. H. Electron Induced Surface Reactions of the Organometallic Precursor Trimethyl-(Methylcyclopentadienyl)Platinum(IV). *J. Phys. Chem. C* **2009**, *113*, 2487−2496.
(22) Randolph, S. J.; Fowlkes, J. D.; Rack, P. D. Focused, Nanoscale Electron-Beam-Induced Deposition and Etching. *Crit. Rev. Solid State Mater. Sci.* **2006**, *31*, 55−89.
(23) Schaefer, J.; Hoelzl, J. A Contribution to the Dependence of Secondary Electron Emission from the Work Function and Fermi Energy. *Thin Solid Films* **1972**, *13*, 81−86.
(24) Botman, A.; de Winter, D. A. M.; Mulders, J. J. L. Electron-Beam-Induced Deposition of Platinum at Low Landing Energies. *J. Vac. Sci. Technol., B: Microelectron. Nanometer Struct.–Process., Meas., Phenom.* **2008**, *26*, 2460−2463.
(25) Hoyle, P. C.; Cleaver, J. R. A.; Ahmed, H. Ultralow-energy Focused Electron Beam Induced Deposition. *Appl. Phys. Lett.* **1994**, *64*, 1448−1450.
(26) Engmann, S.; Stano, M.; Papp, P.; Brunger, M. J.; Matejčík, Š.; Ingólfsson, O. Absolute Cross Sections for Dissociative Electron Attachment and Dissociative Ionization of Cobalt Tricarbonyl Nitrosyl in the Energy Range from 0 eV to 140 eV. *J. Chem. Phys.* **2013**, *138*, 044305.
(27) May, O.; Kubala, D.; Allan, M.; Viggiano, A. A.; Rekha, G. K.; Stevens, A. E.; Tolstikov, G. A. Dissociative Electron Attachment to $Pt(PF_3)_4$ — a Precursor for Focused Electron Beam Induced Processing (FEBIP). *Phys. Chem. Chem. Phys.* **2012**, *14*, 2979−2982.
(28) Wnorowski, K.; Stano, M.; Matias, C.; Denifl, S.; Barszczewska, W.; Matejčík, Š. Low-Energy Electron Interactions with Tungsten Hexacarbonyl - $W(CO)_6$. *Rapid Commun. Mass Spectrom.* **2012**, *26*, 2093−2098.
(29) Ingólfsson, O. Low Energy Electron−Induced Dissociation. In *Low-Energy Electrons: Fundamentals and Applications*; Ingólfsson, O., Ed.; Pan Stanford Publishing Pte. Ltd.: Singapore, 2019; pp 47−120.
(30) Knights, A. P.; Coleman, P. G. Secondary Electron Emission from Ag(100) Stimulated by Positron and Electron Impact. *Appl. Surf. Sci.* **1995**, *85*, 43−48.
(31) Matejčík, Š.; Foltin, V.; Stano, M.; Skalný, J. D. Temperature Dependencies in Dissociative Electron Attachment to CCl_4, CCl_2F_2, $CHCl_3$ and $CHBr_3$. *Int. J. Mass Spectrom.* **2003**, *223*−*224*, 9−19.
(32) Dressler, R.; Allan, M. Energy Partitioning in the O^-/CO_2 Dissociative Attachment. *Chem. Phys.* **1985**, *92*, 449−455.
(33) Bjarnason, E. H.; Ómarsson, B.; Engmann, S.; Ómarsson, F. H.; Ingólfsson, O. Dissociative Electron Attachment to Titatinum Tetrachloride and Titanium Tetraisopropoxide. *Eur. Phys. J. D* **2014**, *68*, 121.
(34) Rosenberg, S. G.; Barclay, M.; Fairbrother, D. H. Electron Beam Induced Reactions of Adsorbed Cobalt Tricarbonyl Nitrosyl ($Co(CO)_3NO$) Molecules. *J. Phys. Chem. C* **2013**, *117*, 16053−16064.
(35) Ipolyi, I.; Michaelis, W.; Swiderek, P. Electron-Induced Reactions in Condensed Films of Acetonitrile and Ethane. *Phys. Chem. Chem. Phys.* **2007**, *9*, 180−191.
(36) Friedman, J. F.; Miller, T. M.; Friedman-Schaffer, J. K.; Viggiano, A. A.; Rekha, G. K.; Stevens, A. E. Electron Attachment to $Ni(PF_3)_4$ and $Pt(PF_3)_4$. *J. Chem. Phys.* **2008**, *128*, 104303.
(37) Allan, M. Electron Scattering in $Pt(PF_3)_4$: Elastic Scattering, Vibrational, and Electronic Excitation. *J. Chem. Phys.* **2011**, *134*, 204309.
(38) Landheer, K.; Rosenberg, S. G.; Bernau, L.; Swiderek, P.; Utke, I.; Hagen, C. W.; Fairbrother, D. H. Low-Energy Electron-Induced Decomposition and Reactions of Adsorbed Tetrakis-(Trifluorophosphine)Platinum [$Pt(PF_3)_4$]. *J. Phys. Chem. C* **2011**, *115*, 17452−17463.
(39) Engmann, S.; Stano, M.; Matejčík, Š.; Ingólfsson, O. The Role of Dissociative Electron Attachment in Focused Electron Beam Induced Processing: A Case Study on Cobalt Tricarbonyl Nitrosyl. *Angew. Chem., Int. Ed.* **2011**, *50*, 9475−9477.
(40) Rosenberg, S. G.; Barclay, M.; Fairbrother, D. H. Electron Induced Reactions of Surface Adsorbed Tungsten Hexacarbonyl ($W(CO)_6$). *Phys. Chem. Chem. Phys.* **2013**, *15*, 4002−4015.
(41) Wnorowski, K.; Stano, M.; Barszczewska, W.; Jówko, A.; Matejčík, Š. Electron Ionization of $W(CO)_6$: Appearance Energies. *Int. J. Mass Spectrom.* **2012**, *314*, 42−48.

https://dx.doi.org/10.1021/acs.jpcc.0c01801
J. Phys. Chem. C 2020, 124, 10593−10604

(42) Thorman, R. M.; Unlu, I.; Johnson, K.; Bjornsson, R.; McElwee-White, L.; Fairbrother, D. H.; Ingólfsson, O. Low Energy Electron-Induced Decomposition of $(\eta^5$-Cp)$Fe(CO)_2Mn(CO)_5$, a Potential Bimetallic Precursor for Focused Electron Beam Induced Deposition of Alloy Structures. *Phys. Chem. Chem. Phys.* **2018**, *20*, 5644−5656.
(43) Unlu, I.; Spencer, J. A.; Johnson, K. R.; Thorman, R. M.; Ingólfsson, O.; McElwee-White, L.; Fairbrother, D. H. Electron Induced Surface Reactions of $(\eta^5$-$C_5H_5)Fe(CO)_2Mn(CO)_5$, a Potential Heterobimetallic Precursor for Focused Electron Beam Induced Deposition (FEBID). *Phys. Chem. Chem. Phys.* **2018**, *20*, 7862−7874.
(44) Thorman, R. M.; Brannaka, J. A.; McElwee-White, L.; Ingólfsson, O. Low Energy Electron-Induced Decomposition of $(\eta^3$-$C_3H_5)Ru(CO)_3Br$, a Potential Focused Electron Beam Induced Deposition Precursor with a Heteroleptic Ligand Set. *Phys. Chem. Chem. Phys.* **2017**, *19*, 13264−13271.
(45) Spencer, J. A.; Brannaka, J. A.; Barclay, M.; McElwee-White, L.; Fairbrother, D. H. Electron-Induced Surface Reactions of η^3-Allyl Ruthenium Tricarbonyl Bromide $[(\eta^3$-$C_3H_5)Ru(CO)_3Br]$: Contrasting the Behavior of Different Ligands. *J. Phys. Chem. C* **2015**, *119*, 15349−15359.
(46) Jurczyk, J.; Brewer, C. R.; Hawkins, O. M.; Polyakov, M. N.; Kapusta, C.; McElwee-White, L.; Utke, I. Focused Electron Beam-Induced Deposition and Post-Growth Purification Using the Heteroleptic Ru Complex $(\eta^3$-$C_3H_5)Ru(CO)_3Br$. *ACS Appl. Mater. Interfaces* **2019**, *11*, 28164−28171.
(47) Spencer, J. A.; Wu, Y.-C.; McElwee-White, L.; Fairbrother, D. H. Electron Induced Surface Reactions of *cis*-$Pt(CO)_2Cl_2$: A Route to Focused Electron Beam Induced Deposition of Pure Pt Nanostructures. *J. Am. Chem. Soc.* **2016**, *138*, 9172−9182.
(48) Ferreira da Silva, F.; Thorman, R. M.; Bjornsson, R.; Lu, H.; McElwee-White, L.; Ingólfsson, O. Dissociation of the FEBID Precursor *cis*-$Pt(CO)_2Cl_2$ Driven by Low-Energy Electrons. *Phys. Chem. Chem. Phys.* **2020**, *22*, 6100−6108.
(49) T.P., R. K..; Barth, S.; Bjornsson, R.; Ingólfsson, O. Structure and Energetics in Dissociative Electron Attachment to $HFeCo_3(CO)_{12}$. *Eur. Phys. J. D* **2016**, *70*, 163.
(50) T.P., R. K..; Unlu, I.; Barth, S.; Ingólfsson, O.; Fairbrother, D. H. Electron Induced Surface Reactions of $HFeCo_3(CO)_{12}$, a Bimetallic Precursor for Focused Electron Beam Induced Deposition (FEBID). *J. Phys. Chem. C* **2018**, *122*, 2648−2660.
(51) T.P., R. K..; Weirich, P.; Hrachowina, L.; Hanefeld, M.; Bjornsson, R.; Hrodmarsson, H. R.; Barth, S.; Fairbrother, D. H.; Huth, M.; Ingólfsson, O. Electron Interactions with the Heteronuclear Carbonyl Precursor $H_2FeRu_3(CO)_{13}$ and Comparison with $HFeCo_3(CO)_{12}$: From Fundamental Gas Phase and Surface Science Studies to Focused Electron Beam Induced Deposition. *Beilstein J. Nanotechnol.* **2018**, *9*, 555−579.
(52) Noh, J. H.; Stanford, M. G.; Lewis, B. B.; Fowlkes, J. D.; Plank, H.; Rack, P. D. Nanoscale Electron Beam-Induced Deposition and Purification of Ruthenium for Extreme Ultraviolet Lithography Mask Repair. *Appl. Phys. A* **2014**, *117*, 1705−1713.
(53) Spencer, J. A.; Rosenberg, S. G.; Barclay, M.; Wu, Y.-C.; McElwee-White, L.; Fairbrother, D. H. Understanding the Electron-Stimulated Surface Reactions of Organometallic Complexes to Enable Design of Precursors for Electron Beam-Induced Deposition. *Appl. Phys. A* **2014**, *117*, 1631−1644.
(54) Spencer, J. A.; Barclay, M.; Gallagher, M. J.; Winkler, R.; Unlu, I.; Wu, Y.-C.; Plank, H.; McElwee-White, L.; Fairbrother, D. H. Comparing Postdeposition Reactions of Electrons and Radicals with Pt Nanostructures Created by Focused Electron Beam Induced Deposition. *Beilstein J. Nanotechnol.* **2017**, *8*, 2410−2424.
(55) Calderazzo, F.; L'Eplattenier, F. Pentacarbonyls Of Ruthenium And Osmium. I. Infrared Spectra And Reactivity. *Inorg. Chem.* **1967**, *6*, 1220−1224.
(56) Johnson, B. F. G.; Johnston, R. D.; Lewis, J. Chemistry of Polynuclear Compounds. Part XV. Halogenocarbonylruthenium Compounds. *J. Chem. Soc. A* **1969**, 792.
(57) Saha, S.; Captain, B. Synthesis and Structural Characterization of Ruthenium Carbonyl Cluster Complexes Containing Platinum with a Bulky N-Heterocyclic Carbene Ligand. *Inorg. Chem.* **2014**, *53*, 1210−1216.
(58) Braun, M.; Marienfeld, S.; Ruf, M.-W.; Hotop, H. High-Resolution Electron Attachment to the Molecules CCl_4 and SF_6 over Extended Energy Ranges with the (EX)LPA Method. *J. Phys. B: At., Mol. Opt. Phys.* **2009**, *42*, 125202.
(59) Wnuk, J. D.; Rosenberg, S. G.; Gorham, J. M.; van Dorp, W. F.; Hagen, C. W.; Fairbrother, D. H. Electron Beam Deposition for Nanofabrication: Insights from Surface Science. *Surf. Sci.* **2011**, *605*, 257−266.
(60) Rosenberg, S. G.; Landheer, K.; Hagen, C. W.; Fairbrother, D. H. Substrate Temperature and Electron Fluence Effects on Metallic Films Created by Electron Beam Induced Deposition. *J. Vac. Sci. Technol., B: Microelectron. Nanometer Struct.–Process., Meas., Phenom.* **2012**, *30*, 051805.
(61) Moulder, J. F.; Chastain, J. *Handbook of X-Ray Photoelectron Spectroscopy : A Reference Book of Standard Spectra for Identification and Interpretation of XPS Data*; Physical Electronics Division, Perkin-Elmer Corp, 1992.
(62) Plummer, E. W.; Salaneck, W. R.; Miller, J. S. Photoelectron Spectra of Transition-Metal Carbonyl Complexes: Comparison with the Spectra of Adsorbed CO. *Phys. Rev. B: Condens. Matter Mater. Phys.* **1978**, *18*, 1673−1701.
(63) Morgan, D. J. Resolving Ruthenium: XPS Studies of Common Ruthenium Materials. *Surf. Interface Anal.* **2015**, *47*, 1072−1079.
(64) Allan, M.; Lacko, M.; Papp, P.; Matejčík, Š.; Zlatar, M.; Fabrikant, I. I.; Kočišek, J.; Fedor, J. Dissociative Electron Attachment and Electronic Excitation in $Fe(CO)_5$. *Phys. Chem. Chem. Phys.* **2018**, *20*, 11692−11701.
(65) Yang, J.; Cui, W.; Li, Y.; Xie, G.; Zhang, N.; Wang, R.; Hu, T.; Zhang, H. Investigation of Argon Ion Sputtering on the Secondary Electron Emission from Gold Samples. *Appl. Surf. Sci.* **2016**, *382*, 88−92.
(66) Rosenberg, S. G.; Barclay, M.; Fairbrother, D. H. Electron Induced Surface Reactions of Organometallic $Metal(Hfac)_2$ Precursors and Deposit Purification. *ACS Appl. Mater. Interfaces* **2014**, *6*, 8590−8601.
(67) Wetzel, R. C.; Baiocchi, F. A.; Hayes, T. R.; Freund, R. S. Absolute Cross Sections for Electron-Impact Ionization of the Rare-Gas Atoms by the Fast-Neutral-Beam Method. *Phys. Rev. A: At., Mol., Opt. Phys.* **1987**, *35*, 559−577.
(68) Zlatar, M.; Allan, M.; Fedor, J. Excited States of $Pt(PF_3)_4$ and Their Role in Focused Electron Beam Nanofabrication. *J. Phys. Chem. C* **2016**, *120*, 10667−10674.
(69) Mendes, M.; Regeta, K.; Ferreira da Silva, F.; Jones, N. C.; Hoffmann, S. V.; García, G.; Daniel, C.; Limão-Vieira, P. Comprehensive Investigation of the Electronic Excitation of $W(CO)_6$ by Photoabsorption and Theoretical Analysis in the Energy Region from 3.9 to 10.8 eV. *Beilstein J. Nanotechnol.* **2017**, *8*, 2208−2218.
(70) Thorman, R. M.; Matsuda, S. J.; McElwee-White, L.; Fairbrother, D. H. Identifying and Rationalizing the Differing Surface Reactions of Low Energy Electrons and Ions with an Organometallic Precursor. *J. Phys. Chem. Lett.* **2020**, *11*, 2006−2013.
(71) Kepp, K. P. Quantitative Scale of Oxophilicity and Thiophilicity. *Inorg. Chem.* **2016**, *55*, 9461−9470.
(72) Rohdenburg, M.; Martinović, P.; Ahlenhoff, K.; Koch, S.; Emmrich, D.; Gölzhäuser, A.; Swiderek, P. Cisplatin as a Potential Platinum Focused Electron Beam Induced Deposition Precursor: NH_3 Ligands Enhance the Electron-Induced Removal of Chlorine. *J. Phys. Chem. C* **2019**, *123*, 21774−21787.

https://dx.doi.org/10.1021/acs.jpcc.0c01801
J. Phys. Chem. C 2020, 124, 10593−10604